Research Square

Preprints are preliminary reports that have not undergone peer review.
They should not be considered conclusive, used to inform clinical practice,
or referenced by the media as validated information.

Optimization of process variables for laser powder bed fusion of creep-resistant P92-type steel

Pavel Dolzhenko
Belgorod National Research University
Ivan Zuiko
Belgorod National Research University
Sergei Borisov
Belgorod National Research University
Ivan Nikitin
Belgorod National Research University
Alexander Kalinenko
Belgorod National Research University
Alexandra Fedoseeva
Belgorod National Research University
Sergei Mironov
S-72@mail.ru

Belgorod National Research University

Research Article

Keywords: Martensitic steels, Laser powder bed fusion (L-PBF), process optimization

Posted Date: July 8th, 2026

DOI: https://doi.org/10.21203/rs.3.rs-10212409/v1

License: This work is licensed under a Creative Commons Attribution 4.0 International License.
Read Full License

Additional Declarations: No competing interests reported.

Optimization of process variables for laser powder bed fusion of creep-resistant P92-type steel

Type P92 steels belong to a recent generation of martensitic steels, which exhibit excellent creep rupture strength and oxidation resistance at extreme steam parameters. Hence, the application of this material in the power generation industry allows drastically improving the plant energy efficiency. Given the significant potential of these steels, it is of interest to evaluate their suitability for an advanced laser powder bed fusion (L-PBF) technology. This study focused on the optimization of L-PBF variables in order to achieve a porosity-free condition. To this end, the key process variables were varied, including laser power, laser scanning rate, hatch distance, and protective gas. It was found that L-PBF is suitable for the manufacturing of samples with residual porosity below 0.1%. The optimal L-PBF condition included a laser power of 250 W, a laser scanning rate of 1 m/s, a hatch spacing of 80 μm, and nitrogen shielding.

Keywords: Martensitic steels; Laser powder bed fusion (L-PBF); process optimization

1. Introduction

The P92-type steels are well-established creep-resistant martensitic steels. Thorough optimization of both the chemical composition and microstructural design of this material provided an excellent balance among the solid-solution, grain-boundary, and precipitation strengthening mechanisms. Accordingly, P92 steels exhibit excellent creep rupture strength and oxidation resistance [e.g., 1-3]. Moreover, a combination of a relatively low thermal expansion coefficient and a comparatively high thermal conductivity in these steels permits decreasing thermal stresses, which may arise during extreme fluctuations. Hence, the application of this material in the power generation industry allows the power plants to operate at relatively high steam parameters, particularly the critical temperatures of 585-600 ºC and pressures up to 25 MPa [e.g., 4-6]. This vastly improves the plant energy efficiency and reduces carbon emission. In addition to the thermal power plants, P92 steels are also utilized in chemical processing, the oil and gas industries, and are even considered as a potential structural material for advanced reactor systems in nuclear power [e.g., 7-9].

Given the significant potential of these steels, it is important to access their suitability for additive manufacturing, particularly in relation to laser powder bed fusion (L-PBF) [e.g., 10-12]. This advanced technology may be applied for the fabrication of complex-shaped parts, including turbine blades, pressure vessel stiffeners, and nuclear reactor internals, which should withstand the extreme temperature and pressure environment. To this end, however, the built parts should exhibit a nearly 100% density and a tempered-martensite microstructure.

A review of the available scientific literature in the Scopus database revealed very little work on the L-PBF of P92-type steels [13-19]. These studies have conclusively demonstrated the feasibility of this technology for manufacturing the parts with excellent

mechanical properties. On the other hand, a comprehensive examination of the optimal processing window for L-PBF of such steel is not available in the scientific literature, to the best of the authors' knowledge. Hence, the present study was undertaken to fill this gap in our knowledge.

2. Experimental

2.1 Program material

The program material used in the present study was a type of P92 steel developed by the authors. The feedstock material for L-PBF was produced at JSC POLEMA using an argon atomization technique and supplied as metallic powder. The nominal chemical composition of the received powder batch is given in Table 1.

Table 1. The nominal chemical composition of the received powder material (wt.%)

Fe	C	Si	Mn	Cr	Co	W	Mo	Nb	V	Cu	S	P	N
Bal.	0.018	0.31	0.25	8.15	3.1	2.1	0.58	0.1	0.1	0.1	0.0048	0.03	0.01

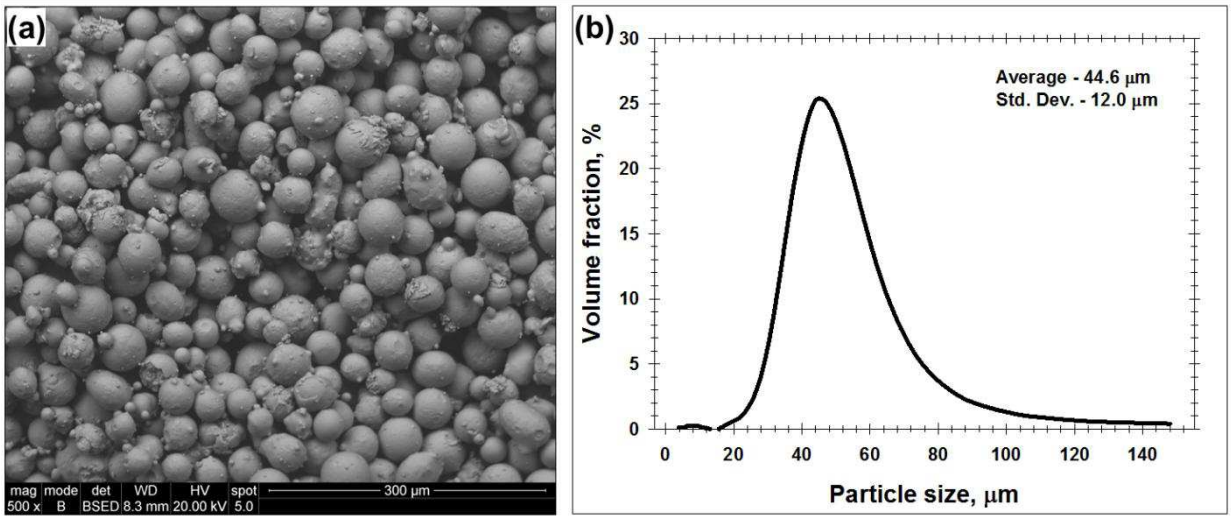


Figure 1. (a) Typical morphology and (b) particle-size distribution of the supplied powder

The received powder material was mainly represented by the nearly spherical particles, which typically contained satellites (Fig. 1a). From the broad perspective, the particle morphology was broadly similar to that of typical gas-atomized martensitic steels reported in the scientific literature [e.g., 20, 21]. The median particle diameter was measured to be ≈45 μm (Fig. 1b), while the percentile particle diameters were D_{10} ≈29 μm, D_{50} ≈42 μm, and D_{90} ≈62 μm.

In greater detail, the characterization of the powder material has been provided elsewhere [22].

2.2 L-PBF procedure

The L-PBF experiments were performed on a ProX DMD 200 machine (3D Systems) using a laser beam with a diameter of ≈80 μm. To establish the optimal L-PBF conditions, three series of L-PBF trials were conducted, as shown in Table 2. The variations included laser power (ranging from 100 to 300 W), laser scanning rate (from 0.5 to 2.5 m/s), hatch distance (50 or 80 μm), and a type of shielding gas (argon or nitrogen). The examined ranges of the laser power and scanning rate encompassed the entire intervals permitted by the ProX DMD 200 machine. The hatch distance of 80 μm was nearly equivalent to the laser beam diameter, while that of 50 μm provided ≈50% overlap between neighboring laser tracks.

Table 2. L-PBF variables applied in the present study

Laser power, W	Laser scanning rate, m/s	Hatch distance, μm	Volumetric energy density , Joule/mm^3	Shielding gas
100	2.5	50	26.7	Argon
150			40.0	
200			53.3	
250			66.7	
300			80.0	
100	2.0		33.3	
150			50.0	
200			66.7	
250			83.3	
300			100.0	
100	1.5		44.4	
150			66.7	
200			88.9	
250			111.1	
100	1.0		66.7	
150			100.0	
200			133.3	
250			166.7	
300			200.0	
100	0.5		133.3	
100	2.5	50	26.7	Nitrogen
150			40.0	
200			53.3	
250			66.7	
300			80.0	
100	2.0		33.3	
150			50.0	
200			66,7	
250			83.3	
300			100.0	
100	1,5		44.4	

150			66.7	
200			88.9	
250			111.1	
100			66.7	
150			100.0	
200	1.0		133.3	
250			166.7	
300			200.0	
100	0.5		133.3	
100			17.1	
150			25.6	
200	2.5		34.2	
250			42.7	
300			51.3	
100			21.4	
150			32.1	
200	2.0		42.7	
250			53.4	
300			64.1	
100			28.5	
150	1.5	80	42.7	Nitrogen
200			57.0	
250			71.2	
100			42.7	
150			64.1	
200	1.0		85.5	
250			106.8	
300			128.2	
100			85.0	
150	0.5		128.2	
200			170.9	
300	1.0		128.2	

In all cases, the nominal thickness of the powder layer was 30 μm, and a simple parallel scan strategy was used. The latter involved a 90° rotation of the laser scan direction between successive layers.

In total, 75 different regimes were applied. In some cases, however, the L-PBF process was not successful, and so only 63 samples were built. The list of the successful regimes is shown in Table 2.

A typical L-PBF coordinate system was adopted, which included the building direction (BD), the motion direction of powder roll (RD), and the transverse direction (TD). In all cases, the cuboidal samples with dimensions of 20×10×5 mm^3 (RD×TD×BD) were built.

2.3 Characterization

The characterization of the built samples was mainly focused on the analysis of residual porosity, which was measured using both the Archimedes method and the optical metallography technique. Moreover, the broad aspects of the evolved microstructure were examined in selected cases.

The Archimedes density measurements were performed using a Porotech ASP 3.1 automated porosimeter in an n-octane liquid medium with a weighting accuracy of ±0.0001 g. For the metallographic analysis of porosity, the built samples were cut in half along the BD, so the observations were focused on the TD×BD plane. The microstructural specimens were mounted into a conductive resin and mechanically polished using standard metallographic procedures. A final surface finish was achieved employing ≈24-h vibratory polishing with a commercial OP-S colloidal silica suspension. The porosity measurements were carried out using an Olympus GX51 optical microscope equipped with SIAMS 800 software.

Microstructural observations were conducted in the vibratory-polished samples and involved backscatter electron (BSE) imaging and the electron backscatter diffraction (EBSD) technique. In both cases, the scanning-electron microscope FEI Quanta 600 was used.

3. Results and Discussion

3.1. Preliminary analysis

The appearance of the top surface of the built samples as a function of L-PBF conditions is shown in Fig. 2a (the process variables are indicated in the top right corner of the images). The samples manufactured at a combination of a low laser power and a high scanning rate (i.e., a low volumetric energy density) exhibited a grainy matte characteristic, thus suggesting a powder-type structure. However, with an increase in the power and/or decrease in the scanning rate (i.e., with an enlargement in the energy density), the sample surface tended to become smooth and glossy. Moreover, the laser tacks, inclined ±45^{o} relative to the RD, became visible. These observations suggest that the powder melted during L-PBF, followed by the subsequent splashing of liquids during the motion of the laser beam.

The effect of the volumetric energy density of the L-PBF process on the relative density of built samples measured by the Archimedes method is summarized in Fig. 2b. In all three experimental trials, observations revealed a broadly similar material behavior. Specifically, the density of the built material grew with the energy density up to

~99% magnitude and then tended to saturate at this level. This trend is typically reported in the scientific literature on L-PBF of martensitic steels [e.g., 23-25].

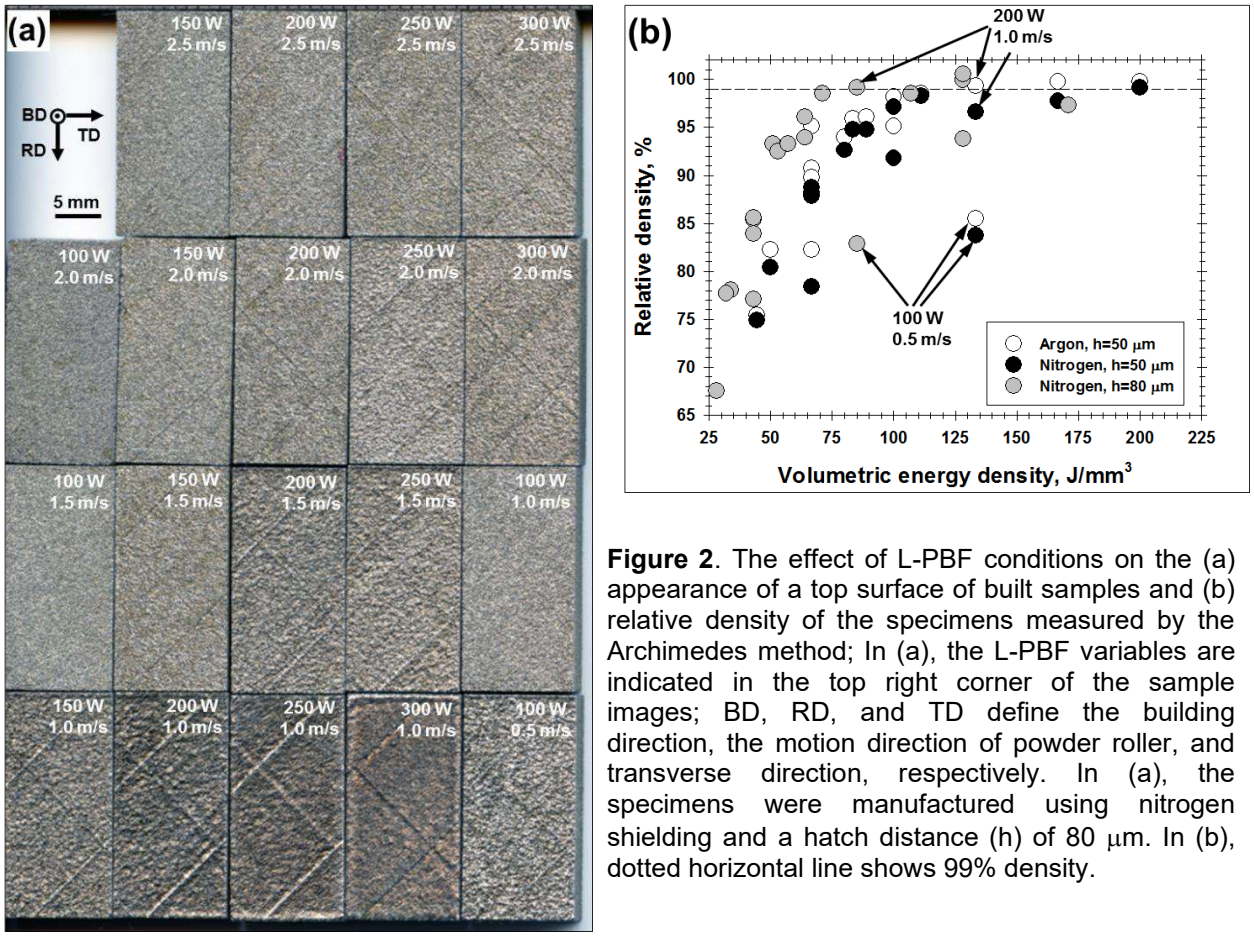


Figure 2. The effect of L-PBF conditions on the (a) appearance of a top surface of built samples and (b) relative density of the specimens measured by the Archimedes method; In (a), the L-PBF variables are indicated in the top right corner of the sample images; BD, RD, and TD define the building direction, the motion direction of powder roller, and transverse direction, respectively. In (a), the specimens were manufactured using nitrogen shielding and a hatch distance (h) of 80 μm. In (b), dotted horizontal line shows 99% density.

A distinct characteristic of the measurements was a significant experimental scattering. Particularly, the samples, which were built at the same volumetric energy density but using a laser power of 100 W, exhibited an extremely low material density (several examples are arrowed in Fig. 2b). This observation suggested that this laser power was insufficient for melting the program material. Thus, even if the volumetric energy density of such L-PBD regimes was nominally high, those only provided powder sintering, which led to increased porosity in the built samples and pronounced experimental scattering. This observation presumably implied that the volumetric energy density is not a comprehensive characteristic of the L-PBF process.

Another important issue was only a minor influence of the L-PBF atmosphere on porosity. Specifically, the specimens manufactured using the same hatch spacing (h) of 50 μm but different shielding atmospheres (argon vs. nitrogen) exhibited broadly overlapping behavior (Fig. 2b). In fact, the use of argon shielding instead of nitrogen provided only a subtle increase in relative density (Fig. 2b). In the high-energy range (>70 J/mm^3), this effect was likely attributable to the relatively low solubility of argon in

steels [26, 27] and the concomitant reduction in gas porosity. In the low-energy interval (<70 J/mm^3), this observation can be explained in terms of the comparatively low thermal conductivity of argon [28-30], i.e., a lower cooling rate and, thus, a longer sintering time.

In contrast, the change in the hatch distance had a significantly greater impact. Specifically, its increase from 50 to 80 μm resulted in a reduction of the volumetric energy density, which provided 1% porosity, from ≈135 J/mm^3 to ≈100 J/mm^3 (Fig. 2b). The potential explanation for this phenomenon is addressed in Section 3.2.

Table 3. Effect of L-PBF variables on the relative density as measured by the Archimedes method

L-PBF variables		**Relative density, %**		
Laser power, W	Laser scanning rate, m/s	Argon shielding, hatch distance of 50 μm	Nitrogen shielding, hatch distance of 50 μm	Nitrogen shielding, hatch distance of 80 μm
250	2.5	95.1	88.2	85.4
300	2.5	93.9	92.6	93.2
150	2.0	82.3	80.4	77.7
200	2.0	90.8	88.7	85.6
250	2.0	95.9	94.7	92.5
300	2.0	98.2	97.1	96.0
100	1.5	75.4	74.9	67.5
150	1.5	89.8	87.8	83.9
200	1.5	96.1	94.8	93.3
250	1.5	98.5	78.4	77.1
150	1.0	95.1	91.8	93.9
200	1.0	99.3	96.6	99.2
250	1.0	99.7	97.7	99.7
300	1.0	99.8	99.2	99.9
100	0.5	85.5	83.7	82.8

Note: The optimal processing window is highlighted in gray

The revealed correlation between the L-PBF variables and the measured density of the built samples is summarized in Table 3. The processing conditions, which provided a 99% relative density, are highlighted in gray. It is seen that the optimal processing window for the examined P92 steel was within the laser power range of 200 to 300 W, with the laser scanning rate of 1 m/s.

3.2. Analysis of discontinuities

3.2.1. Broad aspects

Based on the above-discussed results, the approach, which involved nitrogen shielding and a hatch spacing of 80 μm, was selected as the most promising for a practical use. Hence, the subsequent analysis was focused only on this L-PBF trial.

The low-magnification optical images of the built samples are shown in Fig. 3 as a function of volumetric energy density. In all cases, dark areas within the samples reflected the discontinuities produced during the L-PBF process.

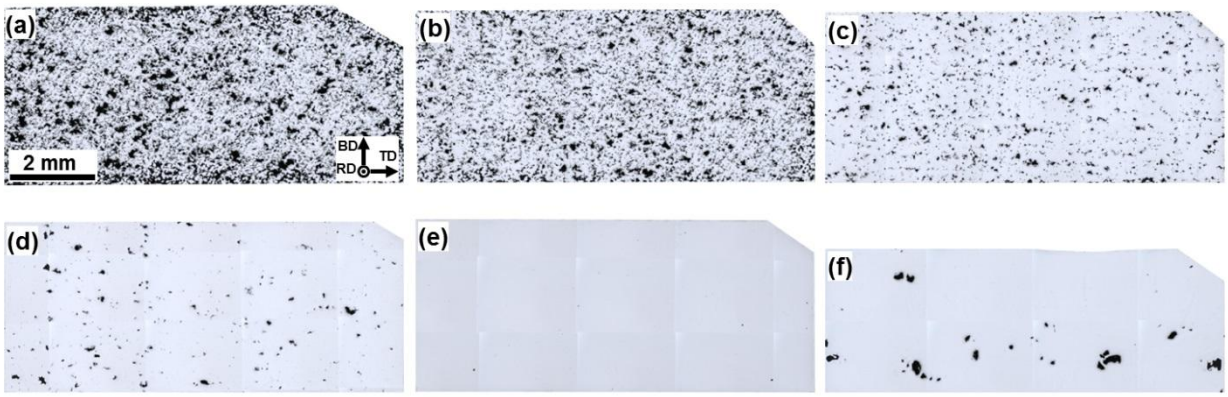


Figure 3. Low-magnification optical images of the polished cross-section of built specimens, which were manufactured under the volumetric energy density of (a) 28.5 J/mm^3, (b) 32.1 J/mm^3, (c) 51.3 J/mm^3, (d) 71.2 J/mm^3, (e) 106.8 J/mm^3, and (f) 200 J/mm^3. In all cases, the specimens were manufactured in nitrogen atmosphere and using a hatch distance of 80 μm. The common scale bar and reference frame are shown in (a). BD, RD, and TD are the building direction, the motion direction of powder roller, and transverse direction, respectively.

At the lowest energy density, an increased concentration of the discontinuities was revealed near the outer edges of the built sample (Fig. 3a). In the remaining cases, however, such macro-scale heterogeneity was not evident, at least from a visual expression. On the other hand, the preferential concentration of discontinuities along the parallel horizontal lines, i.e., virtually along the laser tracks, was revealed (Figs. 3a to c and 3f). This observation was entirely consistent with the scientific literature [e.g., 31, 32].

Moreover, in agreement with the previous works [e.g., 23-25], an increase in volumetric energy density led to a gradual elimination of porosity, which nearly completely disappeared at approximately 100 J/mm^3 (Figs. 3a to e).

At extremely large energies (≈200 J/mm^3), however, a sudden increase in porosity was observed (Fig. 3f). Despite this effect also being mentioned in the scientific literature, its origin is not clear. One of the possible explanations may be the splashing of a molten material during laser motion, as mentioned in Section 3.1.

The latter effect was consistent with the positive influence of an increased hatch distance on the residual porosity, as mentioned in Section 3.1. The partial overlapping of neighboring laser tracks, when using a hatch spacing of 50 μm, should result in local overheating and thus may promote porosity.

To examine the reliability of the porosity measurements, a comparison of two employed approaches (i.e., the Archimedes method and optical metallography) was provided in Fig. 4.

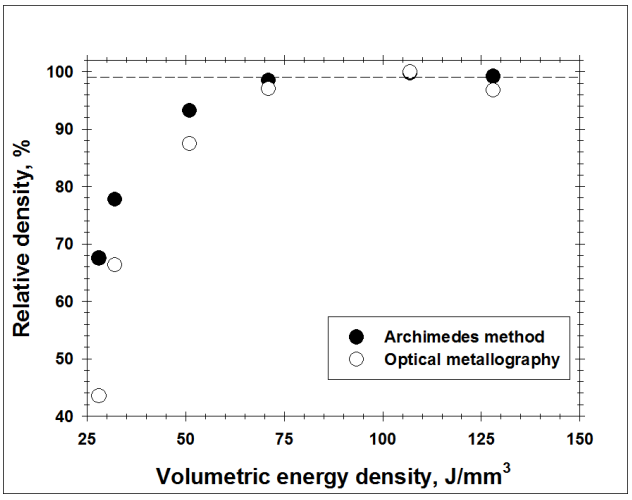


Figure 4. A comparison of the density measurements using the Archimedes method and optical metallography. Note: The specimens were manufactured using nitrogen shielding and a hatch distance of 80 μm; dotted horizontal line shows 99% density.

At the relative density of ~99%, an excellent agreement between two techniques was observed. On the other hand, beyond this range, a considerable discrepancy was revealed. Specifically, the Archimedes method resulted in a significant underestimation of porosity. Moreover, this misfit increased rapidly with the porosity content. The reason for this effect is not clear. Nevertheless, it was concluded that the Archimedes approach is only suitable for an express analysis, while a detailed investigation requires optical observations.

3.2.2. Morphology

The typical morphology of the discontinuities revealed within the built samples was summarized in Fig. 5 as a function of the volumetric energy density. Again, the discontinuities were represented by the dark-contrast areas.

At the energy density below ≈70 J/mm^3, the distinct remnants of the initial powder particles were clearly recognizable (Figs. 5a to c). Consequently, no massive particle melting was occurred within this energy range, leading to the conclusion that the L-PBF process was primarily governed by powder sintering. As a result, the most revealed discontinuities represented the lack-of-fusion defects.

Remarkably, the clear evidence of gas porosity was also found within the survived particles (several examples are arrowed in Figs. 5a to c). These defects likely originated

from the argon-gas atomization of the feedstock powder material and were then inherited during the subsequent L-PBF process.

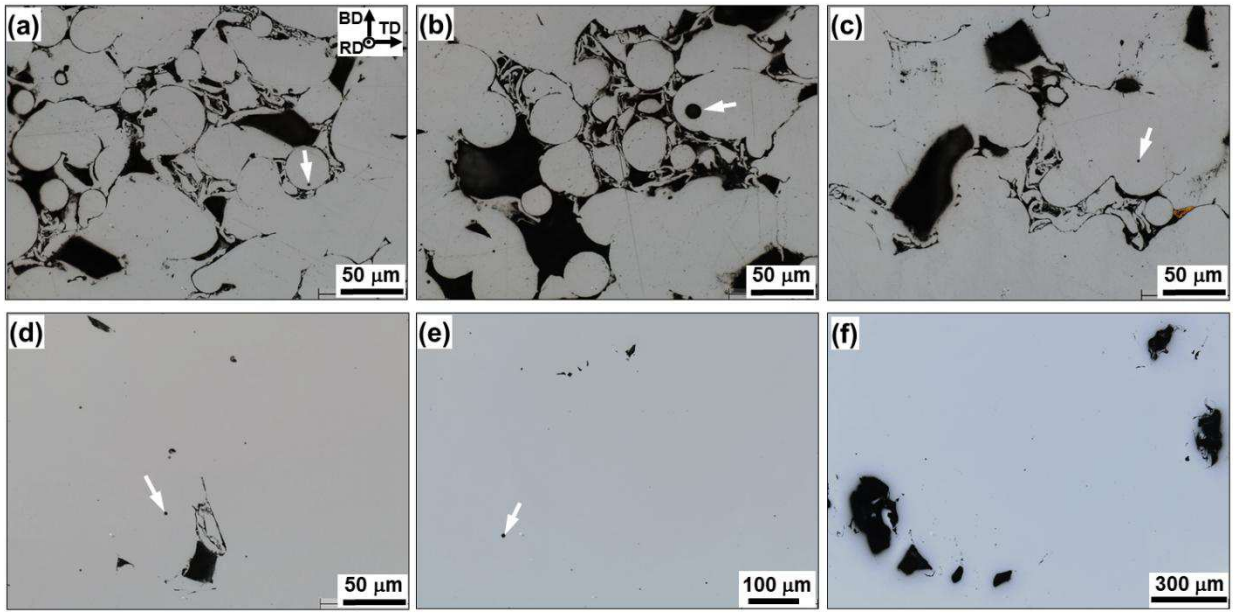


Figure 5. Typical morphology of discontinuities revealed within the additive specimens manufactured under the volumetric energy density of (a) 28.5 J/mm^3, (b) 32.1 J/mm^3, (c) 51.3 J/mm^3, (d) 71.2 J/mm^3, (e) 106.8 J/mm^3, and (f) 200 J/mm^3. Arrows exemplify gas porosity. In all cases, the specimens were manufactured in nitrogen atmosphere and using a hatch distance of 80 μm. The common reference frame is shown in the top right corner of (a). BD, RD, and TD are the building direction, the motion direction of powder roller, and transverse direction, respectively.

In the energy range between ≈70 and ≈100 J/mm^3, the revealed discontinuities included both the lack-of-fusion defects and gas porosity (Figs. 5d to e). No distinct remnants of the original particle structure were revealed, and so the feedstock powder material was likely completely molten during L-PBF.

At extremely high energy density, an abrupt increase in the fraction of coarse discontinuities was found (Fig. 3f). Given the specific morphology of the discontinuities (Fig. 5f), it seems unlikely that those were related to the lack of fusion. Thus, the microstructural observations appear to be consistent with the above hypothesis of the partial splashing of molten material during the high-energy L-PBF.

3.2.3. Size distributions

The effect of volumetric energy density on discontinuity size distribution measured by optical metallography is shown in Fig. 6.

In most cases, the median discontinuity size was close to ~40 μm (Fig. 6a), i.e., it was comparable with the mean particle size of the feedstock powder material (Fig. 1b). Hence, it can be concluded that the revealed porosity was primarily contributed by the lack-of-fusion defects.

The deviation from this trend was revealed solely at the extremely high energy density of ≈200 J/mm^3, where a sudden increase in the size of discontinuities was noted (Fig. 5b). This observation agreed well with the above-mentioned hypothesis that the coarse discontinuities in this sample were unlikely related to the lack of fusion.

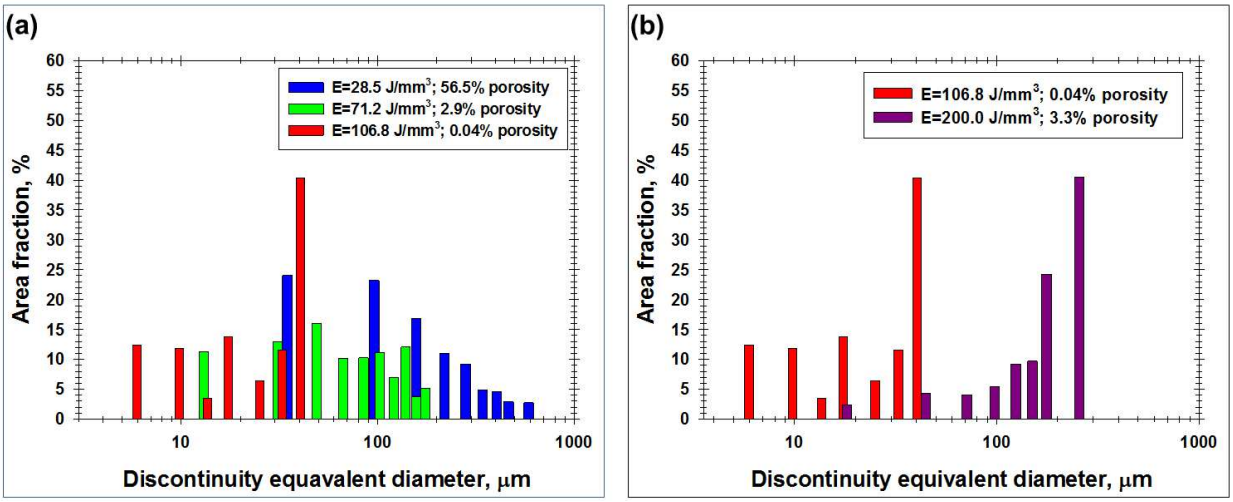


Figure 6. Effect of volumetric energy density on discontinuity size distribution: (a) a low-energy range and (b) a high-energy range. In all cases, statistical data were derived from the specimens manufactured in nitrogen shielding and using a hatch distance of 80 μm.

3.3. Microstructure

Based on the above-discussed results, the following combination of L-PBF variables was selected to be optimal for the program material: laser power of 250 W, laser scanning rate of 1 m/s, a hatch spacing of 80 μm, and nitrogen shielding. The porosity of this material condition, as measured by metallography, was below 0.1%.

To investigate the broad aspects of the microstructure, which evolved in this material, EBSD measurements and BSE observations were applied. The relevant results were shown in Fig. 7.

A distinct “fish scale” structure was revealed (Fig. 7a). It is believed that such meso-scale structures arise from the localized nature of the melting-to-solidification phenomena that occur during L-PBD, making them characteristic of this process [e.g., 33-35]. In the scientific literature, these cells are sometimes referred to as local molten pools. Remarkably, the typical breadth of the pools was ~100 μm (Fig. 7a), thus being comparable with the diameter of the laser beam (i.e., ≈80 μm). On the other hand, the characteristic depth of the local molten pools essentially exceeded the nominal thickness of the powder layer used in the present study, i.e., 30 μm (Fig. 7a). The latter observation suggested that the material experienced several melting-to-solidification cycles during 3D printing.

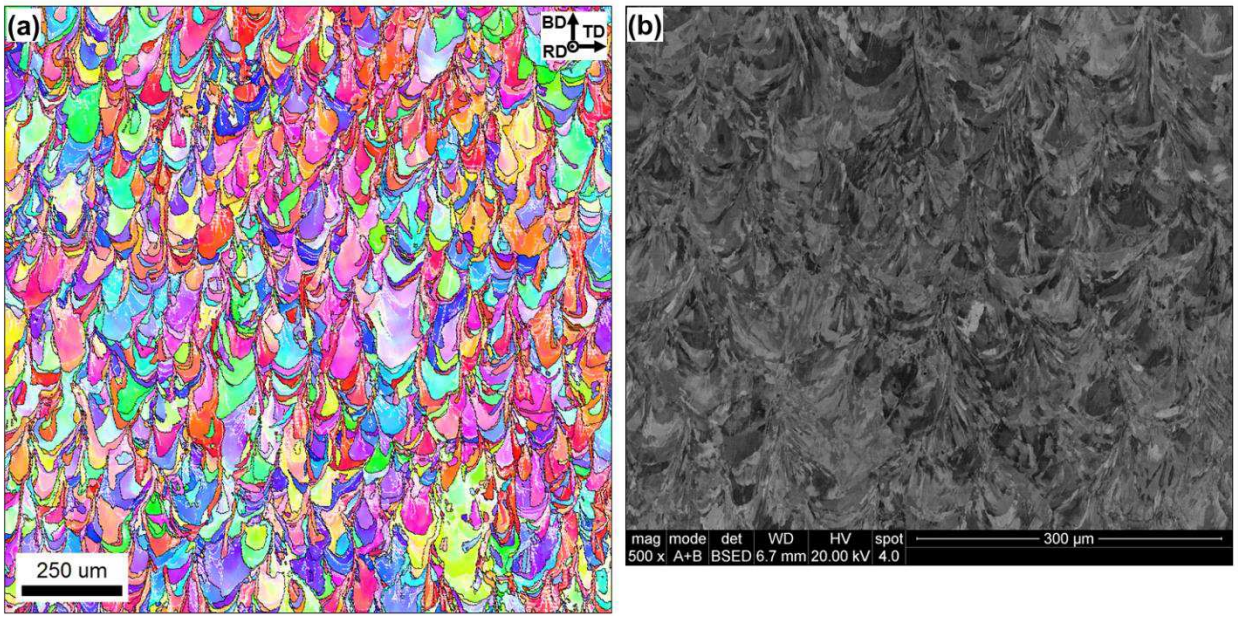


Figure 7. Microstructural observations in the specimen built using the optimal L-PBF condition: (a) low-magnification EBSD map and (b) a higher magnification back-scatter diffraction (BSE) image. In (a), individual pixels are colored according to their crystallographic orientation relative to the building direction, while low-angle boundaries and high-angle boundaries are depicted by white and black lines, respectively. The common reference frame for both figures is shown in the top right corner of (a); BD, RD, and TD are the building direction, the motion direction of the powder roller, and the transverse direction, respectively.

Within the local molten pools, a coarse (sometimes, even single-crystal) grain structure was found (Fig. 7a). BSE imaging showed that the grains typically comprised the columnar-shaped dendrites, which typically nucleated at the pool borders and tended to align with the building direction (Fig. 7b).

Considering the characteristic microstructure morphology, it is highly likely that the microstructure produced during L-PBF was dominated by δ-ferrite. This suggestion was consistent with the literature data on the L-PBD of martensitic steels [e.g., 13-19, 36-38]. The retention of this metastable phase in the built material reflects an extremely high cooling rate, which is intrinsic to the L-PBF process.

Therefore, the L-PBF'ed steel P92, in its as-built condition, is not suitable for direct use in extreme power plant environments. An appropriate heat treatment is necessary. This issue, however, is outside the topic of the present study.

Moreover, the BSE observations of the evolved microstructure at high magnification revealed a significant volume fraction (≈0.3%) of nanoscale features, which were uniformly distributed throughout the built material (Figs. 8a and b). Given the nearly ideal spherical morphology and dark contrast of these structural elements (Fig. 8a), those may represent the nanoscale gas porosity. If so, the metallographic analysis of porosity, which is widely applied in L-PBF, does not reflect the real pattern.

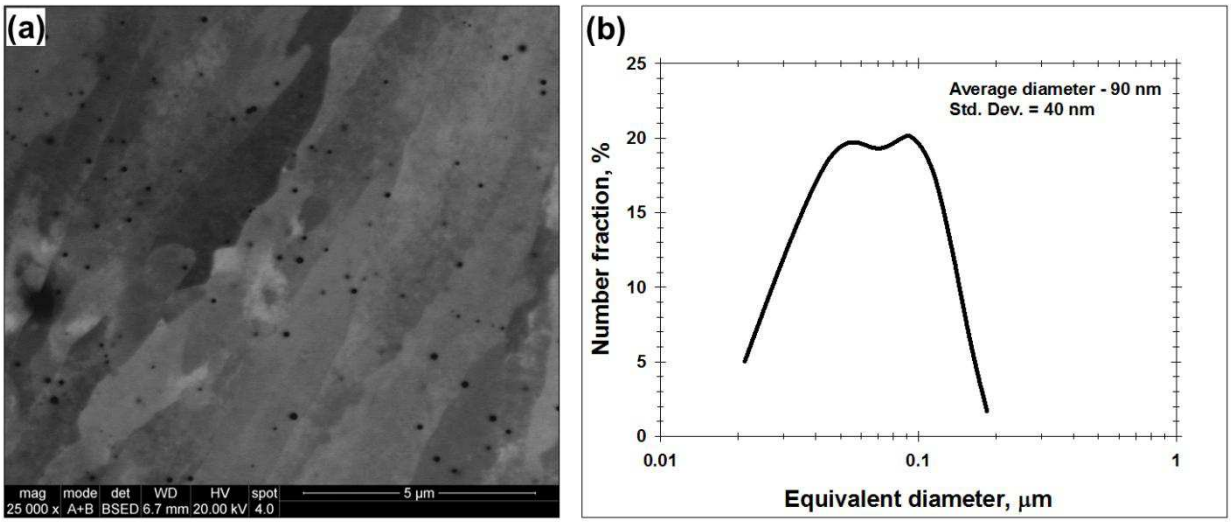


Figure 8. The presumed nanoscale porosity revealed within the specimen built using the optimal L-PBF condition: (a) typical morphology and (b) size distribution. See Section 3.3 for details

On the other hand, an alternative explanation for the revealed structure is the precipitation of second-phase particles during L-PBF. Therefore, transmission-electron microscopy is necessary to clarify the origin of these structural elements.

4. Conclusions

This study was undertaken to evaluate the feasibility of L-PBF technology for 3D printing of advanced P92 creep-resistant steel. The main focus was placed on the production of porosity-free samples. To establish the optimal L-PBF condition, the key process variables were varied, including laser power (ranging from 100 to 300 W), laser scanning rate (from 0.5 to 2.5 m/s), hatch distance (50 or 80 μm), and a type of chamber atmosphere (argon or nitrogen). Moreover, the broad aspects of L-PBD-induced microstructure were also examined. From experimental results, the following conclusions were drawn.

(1) L-PBF is suitable for the manufacturing of samples with residual porosity below 0.1%. The optimal L-PBF condition includes a laser power of 250 W, a laser scanning rate of 1 m/s, a hatch spacing of 80 μm (volumetric energy density of 106.8 J/mm^3), and nitrogen shielding.

(2) L-PBF leads to the formation of an undesirable δ-ferrite structure. Therefore, the as-built products are not proper for direct use. Appropriate heat treatment is necessary.

(3) The laser power of 100 W was found to be insufficient for melting powder material per se, despite even a nominally high volumetric energy density being

provided. Accordingly, the concomitant L-PBF regimes provided only the powder sintering, thus leading to an increased residual porosity.

(4) The chamber atmosphere exerted only a minor influence on porosity. Specifically, the use of argon shielding instead of nitrogen provided only a subtle increase in the relative density of built samples. Conversely, increasing the hatch distance to the laser beam diameter enabled avoiding overheating of the material in overlapping areas, thereby significantly reducing porosity.

(5) At porosity levels exceeding 1%, the accuracy of the Archimedes method was found to be low. Hence, it was concluded that the Archimedes approach is only suitable for an express analysis, while precise measurements require optical metallography.

Conflict of interest

The authors declare no conflict of interest

References

[1] Ennis PJ, Zielinska-Lipiec A, Wachter O, Czyrska-Filemonowicz A (1997) Microstructural stability and creep rupture strength of the martensitic steel P92 for advanced power plant. Acta Materialia 45(12):4901-4907. https://doi.org/10.1016/S1359-6454(97)00176-6.

[2] Ennis PJ, Czyrska-Filemonowicz A (2003) Recent advances in creep-resistant steels for power plant applications. Sadhana 28:709–730. https://doi.org/10.1007/BF02706455

[3] Abe F, Horiuchi T, Taneike M, Sawada K (2004) Stabilization of martensitic microstructure in advanced 9Cr steel during creep at high temperature. Materials Science and Engineering: A 378(1–2):299-303. https://doi.org/10.1016/j.msea.2003.11.073.

[4] Yoshizawa M, Igarashi M, Moriguchi K, Iseda A, Armaki HG, Maruyama K (2009) Effect of precipitates on long-term creep deformation properties of P92 and P122 type advanced ferritic steels for USC power plants. Materials Science and Engineering: A 510–511:162-168. https://doi.org/10.1016/j.msea.2008.05.055.

[5] Yin K, Qiu S, Tang R, Zhang Q, Zhang L (2009) Corrosion behavior of ferritic/martensitic steel P92 in supercritical water. The Journal of Supercritical Fluids 50(3):235-239. https://doi.org/10.1016/j.supflu.2009.06.019.

[6] Hald J (2017) High-alloyed martensitic steel grades for boilers in ultra-supercritical power plants, In: Materials for Ultra-Supercritical and Advanced Ultra-Supercritical Power Plants, Woodhead Publishing, pp 77-97. https://doi.org/10.1016/B978-0-08-100552-1.00003-8.

[7] Topbasi C, Motta AT, Kirk MA (2012) In situ study of heavy ion induced radiation damage in NF616 (P92) alloy. Journal of Nuclear Materials 425(1–3):48-53. https://doi.org/10.1016/j.jnucmat.2011.08.046.

[8] Martynova Y, Moller S, Rasinski M, Matveev D, Freisinger M, Kiss K, Kreter A, Unterberg B, Brezinsek S, Linsmeier Ch (2017) Deuterium retention in RAFM steels after high fluence plasma exposure. Nuclear Materials and Energy 12:648-654. https://doi.org/10.1016/j.nme.2017.05.005.

[9] Topbasi C, Kaoumi D, Motta AT, Kirk MA (2015) Microstructural evolution in NF616 (P92) and Fe–9Cr–0.1C-model alloy under heavy ion irradiation. Journal of Nuclear Materials 466:179-186. https://doi.org/10.1016/j.jnucmat.2015.07.003.

[10] DebRoy T, Wei HL, Zuback JS, Mukherjee T, Elmer JW, Milewski JO, Beese AM, Wilson-Heid A, De A, Zhang W (2018) Additive manufacturing of metallic components – Process, structure and properties. Progress in Materials Science 92:112-224. https://doi.org/10.1016/j.pmatsci.2017.10.001.

[11] Chowdhury S, Yadaiah N, Prakash C, Ramakrishna S, Dixit S, Gupta LR, Buddhi D (2022) Laser powder bed fusion: a state-of-the-art review of the technology, materials, properties and defects, and numerical modelling. Journal of Materials Research and Technology 20:2109-2172. https://doi.org/10.1016/j.jmrt.2022.07.121.

[12] Kotadia HR, Gibbons G, Das A, Howes PD (2021) A review of laser powder bed fusion additive manufacturing of aluminium alloys: Microstructure and properties. Additive Manufacturing 46:102155. https://doi.org/10.1016/j.addma.2021.102155.

[13] Neuberger H, Rey J, Hees M, et al. (2017) Selective laser sintering as manufacturing process for the realization of complex nuclear fusion and high heat flux components. Fusion Science and Technology 72:667-672. https://doi.org/10.1080/15361055.2017.1350521.

[14] Villaret F, Boulnat X, Aubry P, Zollinger J, Fabregue D, Carlan Y (2021) Modelling of delta ferrite to austenite phase transformation kinetics in martensitic steels: Application to rapid cooling in additive manufacturing. Materialia 18:101157. https://doi.org/10.1016/j.mtla.2021.101157.

[15] Zhang Sh, Li K, Zhang W, Ma M, Li M, Xue J, Chen H, Hu R, Liu W (2023) A novel additive manufactured reduced activation ferritic/martensitic steel enhanced by in-situ nanoparticles benefiting from oxygen addition. Scripta Materialia 235:115627. https://doi.org/10.1016/j.scriptamat.2023.115627.

[16] Li Sh., Qiu W, Zhao T, Li A, Tan Y, Wen P, Wu Ch, Du J, Tang J (2023) Microstructure and mechanical properties comparison of ferritic/martensitic steel fabricated by wrought and selective laser melting. Materials Letters 335:133844. https://doi.org/10.1016/j.matlet.2023.133844.

[17] Huang B, Zhai Y, Liu S, Mao X. (2018) Microstructure anisotropy and its effect on mechanical properties of reduced activation ferritic/martensitic steel fabricated by selective laser melting. Journal of Nuclear Materials 500:33-41. https://doi.org/10.1016/j.jnucmat.2017.12.011.

[18] Zhai Y, Huang B, Mao X, Zheng M (2019) Effect of hot isostatic pressing on microstructure and mechanical properties of CLAM steel produced by selective laser melting. Journal of Nuclear Materials 515:111-121. https://doi.org/10.1016/j.jnucmat.2018.12.028.

[19] Liu CY, Tong JD, Jiang MG, Chen ZW, Xu G, Liao HB, Wang P, Wang XY, Xu M, Lao CS (2019) Effect of scanning strategy on microstructure and mechanical properties of selective laser melted reduced activation ferritic/martensitic steel. Materials Science and Engineering: A 766:138364. https://doi.org/10.1016/j.msea.2019.138364.

[20] Ghoncheh MH, Shahriari A, Birbilis N, Mohammadi M (2023) Process-microstructure-corrosion of additively manufactured steels: A review. Critical Reviews in Solid State and Materials Sciences 49:607-717. https://doi.org/10.1080/10408436.2023.2255616

[21] Zai L, Zhang C, Wang Y, Guo W, Wellmann D, Tong X, Tian Y (2020) Laser powder bed fusion of precipitation-hardened martensitic stainless steels: A review. Metals 10 (2):255-280. https://doi.org/10.3390/met10020255

[22] Dolzhenko P, Borisov S, Nikitin I, Kalinenko A, Tkacheva Yu, Zuiko I, Fedoseeva A, Mironov S (2026) Structure of powdered creep-resistant P92 steel produced by the argon atomization technique. Next Materials 11:101928. https://doi.org/10.1016/j.nxmate.2026.101928.

[23] Ozsoy A, Yasa E, Keles M, Tureyen EB (2021) Pulsed-mode selective laser melting of 17-4 PH stainless steel: Effect of laser parameters on density and mechanical properties. Journal of Manufacturing Processes 68A:910-922, https://doi.org/10.1016/j.jmapro.2021.06.017

[24] Zhao D, Guo Y, Lai R, Wen Y, Wang P, Liu C, Chen Z, Yang C, Li S, Chen W, Liu Z (2022) Abnormal three-stage plastic deformation in a 17-4 PH stainless steel fabricated by laser powder bed fusion. Materials Science and Engineering: A 858:144160. https://doi.org/10.1016/j.msea.2022.144160.

[25] Irrinki H, Dexter M, Barmore B, Enneti R, Pasebani S, Badwe S, Stitzel J, Malhotra R, Atre SV (2016) Effects of powder attributes and laser powder bed fusion (L-PBF) process conditions on the densification and mechanical properties of 17-4 PH stainless steel. JOM 68:860–868. https://doi.org/10.1007/s11837-015-1770-4

[26] Wu Z, Basu D, Meyer JLL, Larson E, Kuo R, Beuth J, Rollett A (2021) Study of powder gas entrapment and its effects on porosity in 17-4 PH stainless steel parts fabricated in laser powder bed fusion. JOM 73:177–188, https://doi.org/10.1007/s11837-020-04491-z

[27] Basu D, Wu Z, Meyer JLL, Larson E, Kuo R, Rollett A (2021) Entrapped gas and process parameter-induced porosity formation in additively manufactured 17-4 PH stainless steel. Journal of Materials Engineering and Performance 30:5195–5202, https://doi.org/10.1007/s11665-021-05695-3

[28] Murr LE, Martinez E, Hernandez J, Collins S, Amato KN, Gaytan SM, Shindo PW (2012) Microstructures and properties of 17-4 PH stainless steel fabricated by selective laser melting. Journal of Materials Research and Technology 1:167-177. https://doi.org/10.1016/S2238-7854(12)70029-7

[29] Nezhadfar PD, Anderson-Wedge K, Daniewicz SR, Phan N, Shao S, Shamsaei N (2020) Improved high cycle fatigue performance of additively manufactured 17-4 PH stainless steel via in-process refining micro-/defect structure. Additive Manufacturing 36:101604. https://doi.org/10.1016/j.addma.2020.101604.

[30] Murr LE, Gaytan SM, Ramirez DA, Martinez E, Hernandez J, Amato KN, Shindo PW, Medina FR, Wicker RB (2012) Metal fabrication by additive manufacturing using laser and electron beam melting technologies. Journal of Materials Science and Technology 28:1-14. https://doi.org/10.1016/S1005-0302(12)60016-4

[31] Kim YH, Kim MK, Suhr J, Lee T, Kim MK (2024) Exploring the effect of heat treatment on the mechanical performance of 17-4PH stainless steel specimens fabricated by metal additive manufacturing. Experimental mechanics 64:1333–1342. https://doi.org/10.1007/s11340-024-01089-3

[32] McWilliams B, Pramanik B, Kudzal A, Taggart-Scarff J (2018) High strain rate compressive deformation behavior of an additively manufactured stainless steel. Additive Manufacturing 24:432-439. https://doi.org/10.1016/j.addma.2018.09.016

[33] Yao L, Huang S, Ramamurty U, Xiao Z (2021) On the formation of “Fish-scale” morphology with curved grain interfacial microstructures during selective laser melting of dissimilar alloys. Acta Materialia 220:117331. https://doi.org/10.1016/j.actamat.2021.117331.

[34] Li H, Yang Q, Yan J, Liu B, Liu Y (2024) Microstructural evolution and mechanical properties of maraging steel by additive manufacturing. Materials Science and Engineering: A 915:147201. https://doi.org/10.1016/j.msea.2024.147201.

[35] Kultz Unti LF, Aota LS, Jardini AL, Tschiptschin AP, Sandim HRZ, Jagle EA, Zilnyk KD (2021) Microstructural characterization of 15-5PH stainless steel processed by laser powder-bed fusion. Materials Characterization 181:111485. https://doi.org/10.1016/j.matchar.2021.111485.

[36] Vunnam S, Saboo A, Sudbrack C, Starr TL (2019) Effect of powder chemical composition on the as-built microstructure of 17-4 PH stainless steel processed by selective laser melting. Additive Manufacturing 30:100876. https://doi.org/10.1016/j.addma.2019.100876

[37] Moyle MS, Haghdadi N, Liao XZ, Ringer SP, Primig S (2022) On the microstructure and texture evolution in 17-4 PH stainless steel during laser powder bed fusion: Towards textural

design. Journal of Materials Science and Technology 117:183-195. https://doi.org/10.1016/j.jmst.2021.12.015

[38] Alnajjar M, Christien F, Wolski K, Bosch C (2019) Evidence of austenite by-passing in a stainless steel obtained from laser melting additive manufacturing. Additive Manufacturing 25:187-195. https://doi.org/10.1016/j.addma.2018.11.004